

A three-dimensional regional modeling study of the impact of clouds on sulfate distributions during TRACE-P

C. Kittaka,¹ R. B. Pierce,² J. H. Crawford,² M. H. Hitchman,³ D. R. Johnson,³ G. J. Tripoli,³ M. Chin,⁴ A. R. Bandy,⁵ R. J. Weber,⁶ R. W. Talbot,⁷ and B. E. Anderson²

Received 8 November 2003; revised 5 April 2004; accepted 15 April 2004; published 25 June 2004.

[1] The University of Wisconsin Nonhydrostatic Modeling System (UWNMS) is combined with an aqueous sulfur chemistry module to simulate the sulfate transport in east Asia during the Transport and Chemical Evolution Over the Pacific (TRACE-P) period. The simulated results are compared with in situ and satellite measurements collected during the TRACE-P period. The comparisons showed overestimates of sulfate mixing ratios by 20% between 1 and 6 km and underestimates by 30% near the surface and by 50% above 6 km. The comparisons of the sulfate mixing ratios between the simulation and the measurements for a case study of a convective system showed an excellent agreement in the background sulfate mixing ratios. The simulated sulfate mixing ratios in cloudy regions, however, were underestimated by a factor of 2. Volume-integrated sulfate mass in the model domain is calculated. Significant amounts of sulfate (volume-integrated mass 1.5×10^6 to 7.5×10^6 kg) are released into air after being produced in clouds through the oxidation of sulfur dioxide by hydrogen peroxide. Instantaneous sulfate mass within clouds varies from 0.2×10^6 to 3.5×10^6 kg. Sulfate mass removed through precipitation is in the ranges between 0.01×10^6 and 1.8×10^6 kg. Sulfate mass in ice clouds was 2 orders of magnitude smaller than that in liquid clouds. This study shows that the sulfate input to the atmosphere exceeds the sulfate removed from the atmosphere through precipitation in the east Asian region during the TRACE-P. Consequently, east Asia in spring can be an important source region of sulfate and thus can offset the sulfate loss through precipitation scavenging in other regions of the globe.

INDEX TERMS: 0305 Atmospheric Composition and Structure: Aerosols and particles (0345, 4801); 0320 Atmospheric Composition and Structure: Cloud physics and chemistry; 0322 Atmospheric Composition and Structure: Constituent sources and sinks; 0345 Atmospheric Composition and Structure: Pollution—urban and regional (0305); 0368 Atmospheric Composition and Structure: Troposphere—constituent transport and chemistry; **KEYWORDS:** TRACE-P, in-cloud processing

Citation: Kittaka, C., et al. (2004), A three-dimensional regional modeling study of the impact of clouds on sulfate distributions during TRACE-P, *J. Geophys. Res.*, 109, D15S11, doi:10.1029/2003JD004353.

1. Introduction

[2] There has been significant progress in understanding aerosol composition and distributions in the troposphere during the last 20 years. This was in response to strong demands for (1) assessing the aerosol effects on the Earth radiative balance [e.g., *Intergovernmental Panel on Climate Change*, 2001] and (2) reducing air pollution associated with aerosol particles. One important key to this progress is the global coverage provided by satellite observations at high spatial resolution from instruments such as the Moderate-Resolution Imaging Spectroradiometer (MODIS) and the Multiangle Imaging Spectroradiometer (MISR). These observations allow us to monitor global aerosol distributions and to diagnose aerosol column loadings in a retrospective fashion. In situ measurements, which allow direct measurements of chemical composition, are of high

¹Science Applications International Corporation, Hampton, Virginia, USA.

²NASA Langley Research Center, Hampton, Virginia, USA.

³Department of Atmospheric and Oceanic Sciences, University of Wisconsin—Madison, Madison, Wisconsin, USA.

⁴NASA Goddard Space Flight Center, Greenbelt, Maryland, USA.

⁵Department of Chemistry, Drexel University, Philadelphia, Pennsylvania, USA.

⁶School of Earth and Atmospheric Sciences, Georgia Institute of Technology, Atlanta, Georgia, USA.

⁷Institute for the Study of Earth, Oceans and Space, University of New Hampshire, Durham, New Hampshire, USA.

resolution but are sporadic and are suitable for more detailed process studies. An aerosol three-dimensional model can be used to link these two measurements by filling gaps in space and time. Several models have been developed with different representations of chemical composition, particle size distributions, chemical processes in both gas and aqueous phases, and interactions between aerosol particles and also between cloud drops (liquid and ice) and aerosol particles. These range from regional- and cloud-scale models [e.g., *Binkowski and Roselle*, 2003; *Jacobson*, 1997; *Barth et al.*, 2001] to global models [e.g., *Chin et al.*, 2003; *Rasch et al.*, 1997].

[3] One of major constituents of aerosol is sulfate. Sulfate is produced predominantly via the oxidation of sulfur species (sulfur dioxide (SO_2), dimethyl sulfide (DMS), hydrogen sulfide (H_2S), and carbonyl sulfide (OCS)) in the atmosphere. Sulfur dioxide is a major precursor of sulfate in a tropospheric polluted environment. SO_2 is oxidized to sulfate mainly by hydroxyl radical in the gas phase while it is oxidized mainly by hydrogen peroxide (H_2O_2), ozone (O_3) or with iron (Fe(III)) through catalyzed reactions in the aqueous phase [*Seinfeld and Pandis*, 1998; *Kreidenweis et al.*, 1997]. It has been found that the SO_2 oxidation rate in the gas phase is much slower than that in the aqueous phase, i.e., 5% per hour in the gas phase and several hundred percent per hour (an equivalent gas-phase rate of SO_2 conversion to sulfate) in the aqueous phase [*Calvert et al.*, 1985]. Of the three major oxidation pathways in the aqueous phase, hydrogen peroxide is found to be the most effective oxidant under SO_2 abundant conditions [*Kreidenweis et al.*, 1997]. Clouds play a major role in the formation and redistribution of sulfate both locally and globally by providing a unique environment where liquid drops and ice crystals provide an effective medium for chemical reactions and cloud dynamical evolution provides a means for rapid vertical transport of chemical substances [e.g., *Dickerson*, 1987; *Pickering et al.*, 1996].

[4] Sulfate in-cloud production not only adds sulfate mass to the local atmosphere but can also modify the aerosol size distribution. Observations show that populations of aerosol particles that have been processed in clouds have a distinct peak at 0.1–1 μm diameter range in the size distribution [e.g., *Hoppel and Frick*, 1990]. The suggested mechanism for creating this peak in aerosol size distribution is the following. Cloud drops nucleate on cloud condensation nuclei (CCN). As the cloud evolves, the cloud drops absorb water-soluble chemical species, adding mass to the existing chemical species in the drops. When the cloud evaporates, the chemical species may be released as aerosol particles, which are larger in size than the original CCN. In case of SO_2 and H_2O_2 scavenging by clouds, SO_2 may be oxidized by H_2O_2 to produce sulfate. Consequently, aerosol particles processed in clouds have increased sulfate mass and produce an additional peak in the size distribution. Adding sulfate mass to CCN considerably alters the physicochemical and optical properties of CCN by enhancing the hygroscopy of aerosol particles. This leads to the modification of cloud properties and rain persistence, thereby affecting the local radiative and hydrological balance.

[5] East Asia is one of largest source regions of sulfur dioxide in the world, although sulfur dioxide emissions have decreased in recent years due to the slowdown of east

Asian economic development [*Streets et al.*, 2003]. Air masses influenced by these emissions may travel long distances due to the strong westerlies within the Japan jet stream during spring. There is evidence that the east Asian outflow modifies the air mass characteristics downwind and adversely affects the North Pacific and North American air quality [*Jaeglé et al.*, 2003; *Price et al.*, 2003]. As one of the NASA Global Tropospheric Experiment (GTE) efforts, Transport and Chemical Evolution Over the Pacific (TRACE-P) was conducted in spring 2001 to characterize the Asian chemical outflow and to determine its chemical evolution [*Jacob et al.*, 2003]. *Tu et al.* [2003] describe the SO_2 distributions measured during the TRACE-P period under different meteorological conditions. SO_2 concentrations appeared to be influenced (reduced) by clouds during the TRACE-P flights. *Tu et al.* [2003] compared model results obtained from CFORS/STEM-2K1 [*Carmichael et al.*, 2003] with the measured concentrations. The comparisons showed the model poorly represented the SO_2 distributions for the cloudy cases whereas the modeled SO_2 distributions were in good agreement with the measured values for clear sky cases. *Crawford et al.* [2003] also found the observational evidence for cloud scavenging of SO_2 and HNO_3 during the TRACE-P period.

[6] The objective of this paper is to estimate the sulfate production via in-cloud processing in east Asia during the TRACE-P period using the University of Wisconsin Non-hydrostatic Modeling System (UWNMS). UWNMS forms the dynamical core of the regional component of Regional Air Quality Modeling System (RAQMS). RAQMS was used to estimate the tropospheric ozone budget over east Asia during the TRACE-P period [*Pierce et al.*, 2003], also the carbon monoxide transport for the TRACE-P period [*Kiley et al.*, 2003]. *Hitchman et al.* [2004] also use the UWNMS to discuss the TRACE-P flight of 24 March with a focus on transport of alcohols and stratospheric ozone by the convectively induced circulation. For this study, the UWNMS is coupled with an aqueous sulfur chemistry model, which represents the oxidation of SO_2 by H_2O_2 in the aqueous phase. Other competing processes in sulfate production such as gas phase reactions and the oxidation of other sulfur species are considered to be of secondary importance for sulfate in-cloud production and not included in the model. The current version of the sulfur model is part of a broader development effort to incorporate full aerosol chemistry into RAQMS, which currently has full tropospheric gaseous chemistry components. Two global models provide initial and lateral boundary conditions for the regional model simulations. The global component of RAQMS [*Pierce et al.*, 2003] provides H_2O_2 distributions for the initial and boundary conditions of the regional model. Because RAQMS does not employ sulfur chemistry, the Global Ozone Chemistry Aerosol Radiation and Transport (GOCART) model [*Chin et al.*, 2000a, 2000b, 2002, 2003] is used for SO_2 and sulfate initial and boundary conditions of the regional model.

[7] In sections 2 and 3 the components of models used are briefly described. In section 4.1 we characterize the regional model performance of predicting the atmospheric components involved in the sulfate in-cloud production, such as the distributions of SO_2 , sulfate, H_2O_2 , liquid water in clouds, and precipitation by comparing these components

with TRACE-P aircraft measurements and satellite observations. We then describe a case study for 24 March 2001, when the air influenced by a deep convective storm was advected from the east coast of China to the south of the Japan islands (section 4.2.1). We conclude by estimating the contribution of the sulfate in-cloud production to the sulfate budget for the TRACE-P period (sections 4.2.2 and 5).

2. Regional Model Description

2.1. Meteorological Model

[8] The regional meteorological model is University of Wisconsin Nonhydrostatic Modeling System (UWNMS) developed by *Tripoli* [1992]. UWNMS is a three-dimensional nonhydrostatic mesoscale model which uses the quasi-compressible approximation. It has been used for operational mesoscale weather forecasts in the University of Wisconsin-Madison (<http://mocha.meteor.wisc.edu/>). For this study, five water categories, total moisture, water vapor, rain, ice crystal and snow, are carried as separate prognostic variables. Specific mass of total moisture is defined as

$$q_t = q_v + q_c + q_r + q_i + q_s \quad (1)$$

where q_t , q_v , q_c , q_r , q_i , q_s is specific mass of total moisture, water vapor, cloud water, rain, ice crystal and snow, respectively. Liquid cloud water (q_c) is diagnosed using specific masses of the other five water categories. The tendency of bulk specific mass of a water category k is given as

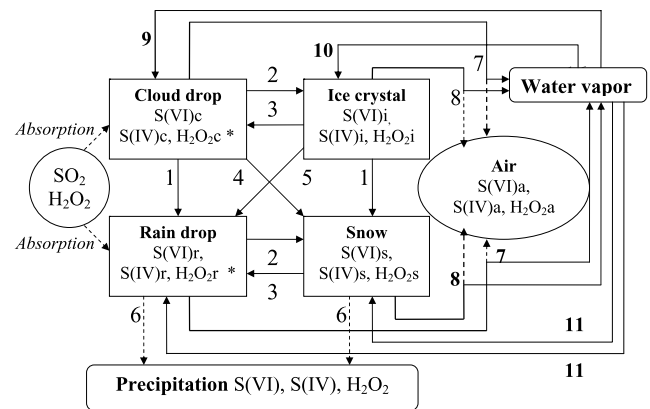
$$\frac{dq_k}{dt} + \frac{1}{\rho} \frac{\partial \rho v_k \delta_{\beta 3} q_k}{\partial x_j} = \left(\frac{dq_k}{dt} \right)_{MP} = +MP_{m \rightarrow k} - MP_{k \rightarrow m} \quad (2)$$

$$\delta_{mn} = \begin{cases} +1 & m = n \\ 0 & m \neq n \end{cases} \quad (3)$$

where q_k is bulk specific mass for category k , ρ is the air density, v_k is the terminal velocity of the hydrometeor, δ is the Kronecker delta, the term with a subscript MP represents the change of the specific mass of a water category k due to the cloud microphysical conversion, $MP_{m \rightarrow k}$ on the right represents a source term of a category k from the conversion of a category m and $MP_{k \rightarrow m}$ is a sink term of a category k that is transformed into a category m . The UWNMS microphysics package includes a comprehensive mixed-phase parameterization [*Flatau et al.*, 1989]. The cloud microphysical processes included are listed in Figure 1. As a prognostic thermodynamic variable, the ice liquid water potential temperature is used and given by

$$\frac{d\theta_{il}}{dt} = \frac{\partial \theta_{il}}{\partial t} + \frac{1}{\rho} \frac{\partial m_j \theta_{il}}{\partial x_j} - \frac{\theta_{il}}{\rho} \frac{\partial m_j}{\partial x_j} = S_{\theta_{il}} + F_{\theta_{il}} \quad (4)$$

where θ_{il} is the ice liquid water potential temperature [*Tripoli and Cotton*, 1981], m_j is the momentum vector, $S_{\theta_{il}}$ is the precipitation source term, and $F_{\theta_{il}}$ represents all turbulent mixing and numerical filters. Subgrid mixing is represented using a modified *Emanuel* [1991] moist convection and one and a half-order turbulent kinetic energy closure. The model is calculated on an Arakawa C grid and a sixth-order



* The pH value is diagnosed using the ion concentrations in cloud and rain drops at every time step.

- | | |
|--|---|
| 1. collision, coalescence and autoconversion | 7. evaporation |
| 2. freezing | 8. sublimation |
| 3. melting | 9. cloud drop nucleation and vapor diffusional growth |
| 4. accretion of cloud water by rain, riming | 10. ice nucleation and vapor diffusional growth |
| 5. accretion of ice by rain | 11. vapor diffusional growth |
| 6. precipitation | |

Figure 1. Schematic diagram of the chemical species associated with cloud microphysical conversion.

flux conservative Crowley scheme is used for advection. The reader is referred to *Tripoli* [1992] for a complete description of the physical parameterizations used to simulate cloud physics, the surface layer, the radiative process, and the subgrid-scale moist convection. The topography is at 10 min \times 10 min resolution and 1° \times 1° climatological values are used for sea surface temperature. An aqueous sulfur chemistry model is incorporated into UWNMS for this study as follows.

2.2. Aqueous Sulfur Chemistry

[9] An aqueous sulfur chemistry model is used to represent the sulfate production in water clouds and subsequent redistribution of sulfate into different water categories due to the cloud microphysical conversion defined by the equation (2). The chemical species included in the model are SO₂ and H₂O₂ in the gas phase, S(IV) (SO₂ and bisulfide (HSO₃⁻)), S(VI) (HSO₄⁻ and SO₄²⁻), and H₂O₂ in the aqueous phase, and S(VI) in the aerosol phase. Additionally, the association of these species with different hydrometeors, such as cloud water, rainwater, ice crystal, and snow, is explicitly predicted in accordance with the cloud microphysical conversion [*Kittaka*, 2001].

[10] The continuity equation of a chemical substance C is given as

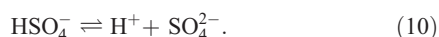
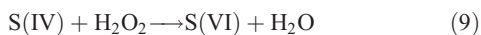
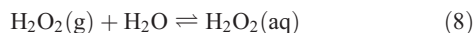
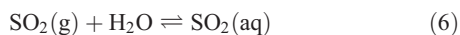
$$\frac{d[C_i]}{dt} = \left(\frac{d[C_i]}{dt} \right)_{\text{ABS}} + \left(\frac{d[C_i]}{dt} \right)_{\text{CHEM}} + \left(\frac{d[C_i]}{dt} \right)_{\text{MP}} \quad (5)$$

where C_i represents the concentration of a chemical substance C associated with a water category (or air) i . C may be S(IV), S(VI), or H₂O₂, whereas the subscript (i) may be a (air), t (total cloud water including water in the liquid and ice phase), r (raindrop), i (ice crystal), or s (snow). S(VI) _{a} is sulfate suspended in air and considered to be in the

aerosol phase (see assumption 5 below). Sulfate within liquid cloud water $S(VI)_c$ is diagnosed using $S(VI)_b$, $S(VI)_r$, $S(VI)_s$, and $S(VI)_c$. $S(IV)_c$ and H_2O_{2c} are also diagnosed. The first term on the right hand side represents the change due to the absorption of chemical substance C into cloud water or rain. The gas scavenging takes place where either cloud or rainwater exists regardless of in-cloud or subcloud. The second term is the change due to chemical reactions listed in equations (6)–(10). The last term represents the change due to cloud microphysical conversion. The removal of chemical species through rainout is also included in this term. Figure 1 shows a schematic diagram of the relation of chemical species in the cloud microphysical conversion.

[11] The primary chemical reaction of the sulfur chemistry model is the oxidation of SO_2 by H_2O_2 . This is the most dominant reaction under cloudy and polluted conditions in the troposphere [Seinfeld and Pandis, 1998].

[12] The chemical equations are



[13] The production rate of sulfate is given as

$$\frac{d[S(VI)]}{dt} = \frac{k_{oxi}[H^+][H_2O_2][HSO_3^-]}{1 + K[H^+]} = -\frac{d[H_2O_2]}{dt} \quad (11)$$

where k_{oxi} is the rate constant and $k_{oxi} = 7.5 \times 10^7 \text{ M}^{-1} \text{ s}^{-1}$ and $K = 13 \text{ M}^{-1}$ at 298K [Seinfeld and Pandis, 1998]. Because $(1 + K[H^+]) \simeq 1$ in the atmospheric environment, equation (11) can be simplified as

$$\frac{d[S(VI)]}{dt} = k_{oxi}[H^+][H_2O_2][HSO_3^-] \quad (12)$$

The temperature dependence of the oxidation rate constant is given as

$$k_{oxi}(T) = k_{oxi}(298) \exp\left[\frac{\Delta H}{R}\left(\frac{1}{298} - \frac{1}{T}\right)\right] \quad (13)$$

where $\Delta H/R = -4430\text{K}$ [Seinfeld and Pandis, 1998].

[14] The sulfate production rate is a function of the concentrations of H_2O_2 , H^+ and HSO_3^- . The concentration of HSO_3^- in turn is a function of H^+ as equation (7) shows. The H_2O_2 absorption into water drops and the chemical reaction with $S(IV)$ is also calculated in the sulfur model. The following assumptions are used to construct the aqueous sulfur chemistry model.

[15] 1. Only a liquid water drop such as a cloud water drop and a raindrop may directly interact with chemical

species. This is a reasonable assumption since laboratory studies have shown that under atmospheric conditions the direct gas uptake by ice crystals may be neglected in comparison to the uptake of gases by water drops [Diehl et al., 1998].

[16] 2. Gases may be absorbed into water drops and subsequently get incorporated into ice through the riming process [Diehl et al., 1998; Borys et al., 1988; Mitchell and Lamb, 1989]. This process is included in the model cloud microphysical transformation.

[17] 3. The chemical species are in equilibrium between the gas phase and liquid phase regardless of drop size. Schwartz [1988] found that interfacial mass transport of H_2O_2 and SO_2 is not a limitation to the in-cloud reaction under conditions of interest and this rules out any drop-size dependence to the kinetics of the reaction for cloud drops. Thus the Henry's law approximation may be applied to determine the concentrations of the chemical species for cloud drops. The same assumption is applied to raindrops. The model time step (2 min) may not be long enough for chemical species to reach the equilibrium state between the gas and aqueous phases for a raindrop, and may introduce a negative bias to the chemical species mixing ratios in the gas phase.

[18] 4. Ambient carbon dioxide (CO_2) with a mixing ratio of 300 ppm is assumed in order to slightly acidify water drops to $pH \simeq 5.6$ before any other chemical reactions take place. This ambient CO_2 mixing ratio remains constant throughout a model run. The pH value in water drop is diagnosed using the ion concentrations in the solution at every time step. In this study the range of pH values is found to be between 4.4 and 5.6.

[19] 5. Sulfate released into air after being produced in clouds is assumed to be in the aerosol phase.

[20] 6. All the chemical substances are assumed to be retained in hydrometeors during freezing of liquid hydrometeors. Stuart and Jacobson [2003] showed that chemicals with very high effective Henry's constants (e.g., HNO_3) are likely to be retained completely, while the retention of chemicals with lower effective Henry's constants depends on pH, temperature, the terminal velocity of the hydrometeor and drop size at freezing. According to their study, SO_2 and H_2O_2 , which have moderate effective Henry's constants, are not completely retained at freezing. Barth et al. [2001] conducted a numerical experiment to determine the effect of degassing during freezing in deep convection on chemical distributions. Their study showed that degassing during freezing results in an increase of the gas in the upper troposphere. Consequently, this assumption may introduce a negative bias in the distributions of gases in the upper troposphere.

[21] 7. The solute distribution in a hydrometeor is assumed to be homogeneous and solute mass transformed into another water category through cloud microphysical conversion is assumed to be proportional to water mass transformed. Although this may introduce inaccuracies in the representation of the conversion of sulfate due to cloud microphysical conversion, there are currently too few quantitative studies to improve the estimate of solute mass.

[22] SO_2 dry deposition, which accounts for a SO_2 removal pathway of about 30% of global SO_2 emissions [Davis et al., 2003], is not included in the model. This is

expected to introduce a high bias in simulated SO₂ mixing ratios.

[23] In order to quantify the in-cloud production of sulfate, we consider two sulfate variables. One is an idealized sulfate tracer, which is subject only to advection and mixing, hereafter S(VI)_{trc}. The other is sulfate in air, S(VI)_a as defined above, which has been subject to in-cloud processing and precipitation in addition to advection and mixing. The difference between these two sulfates accounts for sulfate released into air after being produced in clouds.

2.3. Initial and Boundary Conditions

[24] In order to incorporate H₂O₂ variability within UWNMS, H₂O₂ fields were obtained from global RAQMS simulations and used as initial and lateral boundary conditions for the regional H₂O₂ distribution.

[25] GOCART [Chin *et al.*, 2000a, 2000b, 2002, 2003] is used to initial and lateral boundary conditions for the regional sulfate and SO₂ predictions. GOCART primarily predicts global aerosol distributions of sulfate, dust, organic carbon (OC), black carbon (BC), and sea salt using assimilated meteorological fields from the Goddard Earth Observing System Data Assimilation System (GEOS-DAS). The sulfur species included are SO₂, sulfate, dimethylsulfide (DMS), and methanesulfonic acid (MSA). SO₂ and DMS are subject to oxidation by prescribed oxidants (OH, NO₃, and H₂O₂ from Müller and Brasseur [1995]). The 6 hourly global sulfate and SO₂ distributions (GOCART 2° latitude × 2.5° longitude resolution) and global H₂O₂ distribution (RAQMS 2° latitude × 2° longitude resolution) results are used for initial and lateral boundary conditions. For lateral boundary conditions they are interpolated to every time step of the regional model run and imported to adjust the outer three grid points of the regional model domain. This gives chemical constraints to the regional fields. This is particularly important for SO₂ and sulfate because the large portion of sulfur sources are located farther west of the regional model domain and the sulfur species emitted from the region are known to be advected eastward.

3. TRACE-P Simulation

[26] A simulation of the sulfate transport between 7 March and 3 April 2001 in east Asia was conducted. The domain of the regional model included the eastern half of China, the Korean Peninsula, southeastern Russia, the Japan islands, and northwestern Pacific (see Figure 7). The model domain extended vertically up to 20 km. The spatial resolution of the regional model was 110 km and 0.4 km horizontally and vertically, respectively. The horizontal resolution, which is coarse for a regional model, was chosen by balancing the need to capture the primary emission sources within east Asia and minimizing the amount of computer memory required for the simulation. Furthermore, the 110 km horizontal scale is close to the optimal 1 to 3 ratio of scales for a one-way nesting from the global models (2° × 2.5° for SO₂ and sulfate fields and 2° × 2° for H₂O₂ fields). In order to see the effects of horizontal resolution on the chemical fields, a simulation at higher horizontal resolution 30 km × 30 km in a smaller domain was also conducted. The 6 hourly meteorological fields from the NOAA National Centers for

Environmental Prediction (NCEP) Aviation Model (AVN) 1° × 1° analysis were used for initial and lateral meteorological boundary conditions. The model were initialized at 0600 UT 7 March 2003, and both meteorological and chemical fields were integrated with a 2 min time step. Potential temperature and water vapor predictions in the UWNMS model were relaxed toward the NCEP AVN assimilated fields to give weak meteorological constraints to the regional fields. The 1° gridded SO₂ anthropogenic emissions from the 2000 inventory constructed by Streets *et al.* [2003] were used. The SO₄ emissions are an order of magnitude smaller than those of SO₂ [Davis *et al.*, 2003] and therefore are not included here.

4. Results

4.1. Comparisons With Measurements

4.1.1. Sulfate, Sulfur Dioxide, and Hydrogen Peroxide

[27] Figures 2a–2c show comparisons of SO₂, sulfate, and H₂O₂ mixing ratios at seven different altitude ranges between measured and simulated values for all flights (10 DC-8 flights and 9 P-3B flights for SO₂, 10 DC-8 flights and 10 P-3B flights for sulfate, and 10 DC-8 flights for H₂O₂) from 7 March to 3 April 2001. Fine aerosol non-sea-salt sulfate (NSS SO₄) measurements using mist chamber ion chromatography on DC-8 [Dibb *et al.*, 2003] and sulfate as aerosol bulk ionic composition measurements using particle into liquid sampler (PILS)-ion chromatography on P-3B [Weber *et al.*, 2003] are used and compared with the predicted sulfate S(VI)_a. It should be noted that SO₂ mixing ratios measured on P-3B flights are found to be higher than those on DC-8 according to the intercomparison studies [Eisele *et al.*, 2003]. The 3 hourly instantaneous values are sampled along the flight tracks and interpolated to the in situ measurement time (a 1 min increment). The figures illustrate a monotonic decrease of the mixing ratios of these three species with altitude. At all altitudes the model overestimates sulfur dioxide mixing ratio by a factor of 1.2–3. This is probably due to a lack of SO₂ dry deposition in the model, in addition to uncertainties introduced from the oversimplified representation of the interactions among chemical species and between the chemical species and clouds. The observed variability of sulfur dioxide below 2 km is much larger than the simulated variability. This may be due to the annual average SO₂ emission rate used in the simulation and the neglect of ocean DMS emissions. Sulfate is underestimated near the ground and in the upper troposphere whereas it is overestimated by a factor of 1.2 between 1 and 6 km. Hydrogen peroxide is overestimated by a factor of 1.2–2 at all altitude ranges except between 1 and 4 km, where the simulation results are in good agreement with the measured mixing ratios. The overestimate is larger at higher altitudes. It should be noted that the RAQMS global model generally overestimates H₂O₂ mixing ratios. The combination of the overestimate of sulfur dioxide and the underestimate of sulfate in the boundary layer suggests either lower conversion rates of sulfur dioxide to sulfate or lower liquid water mixing ratio in the model.

[28] Comparisons at six different latitude ranges are shown in Figures 3a–3c. It should be noted that intensive volcanic activity was observed at Miyake-jima (34.08°N, 139.53°E), where a significant amount of SO₂ was emitted

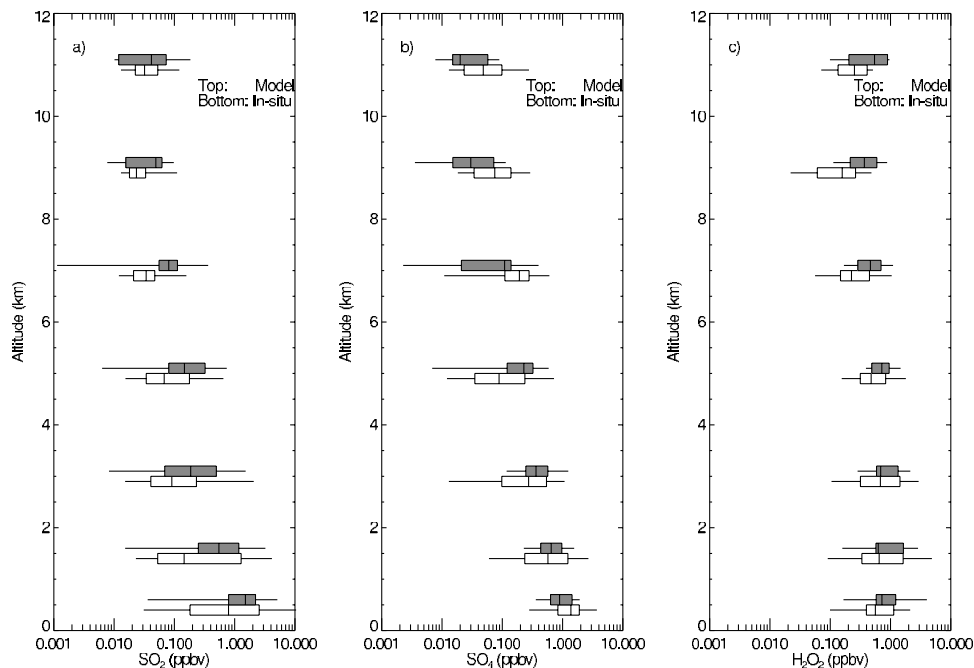


Figure 2. Altitude binned results of model predictions and in situ measurements characterized by their median (vertical line), 50 percentile (box) and 90 percentiles (horizontal lines) for (a) SO₂, (b) sulfate, and (c) H₂O₂.

into the lower troposphere during the TRACE-P period. This volcanic emission was not included in the model simulation. The elevated SO₂ mixing ratios (~10 ppbv) sampled in the southeast of Japan on P-3B flight 14 (18 March) and flight 17 (27 March) were suggested to be directly affected by this volcanic activity according to the mission summary for that flight. Relatively high mixing ratios of SO₂ and sulfate are seen at 27.5°N–42.5°N

whereas high H₂O₂ mixing ratios are found at lower latitudes (≤27.5°N). The H₂O₂ mixing ratios at 35°N are slightly lower than those at the adjacent latitude ranges. This may attribute to the absorption of H₂O₂ into liquid water, which is slightly enhanced at 35°N (not shown).

4.1.2. Cloud and Rain Fields

[29] It is challenging to accurately predict cloud water and precipitation. During in-cloud processing, cloud water

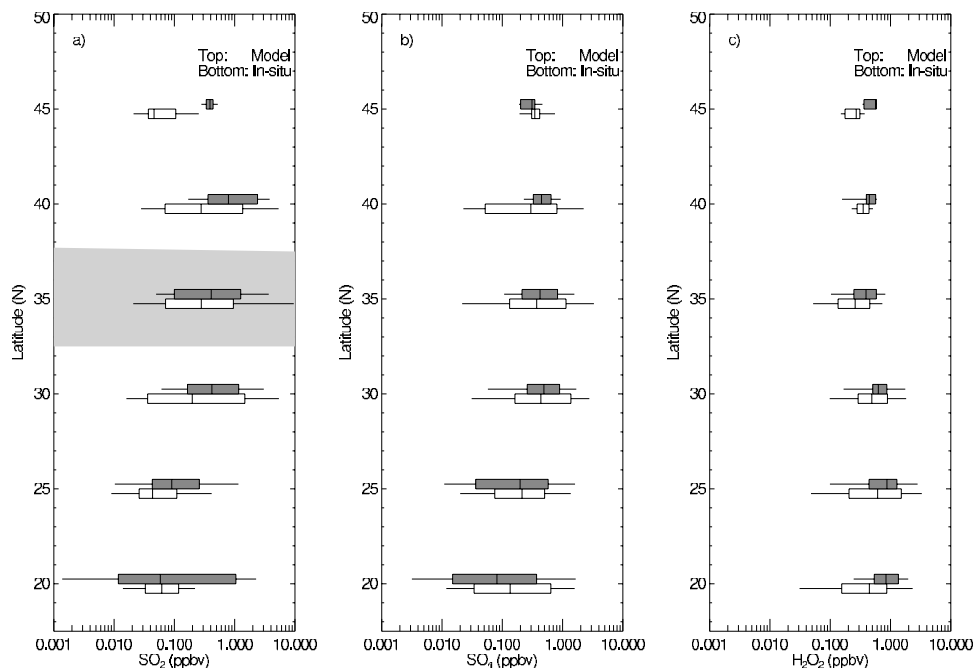


Figure 3. Same as Figure 2 except the mixing ratios are sorted into six different latitudinal bins.

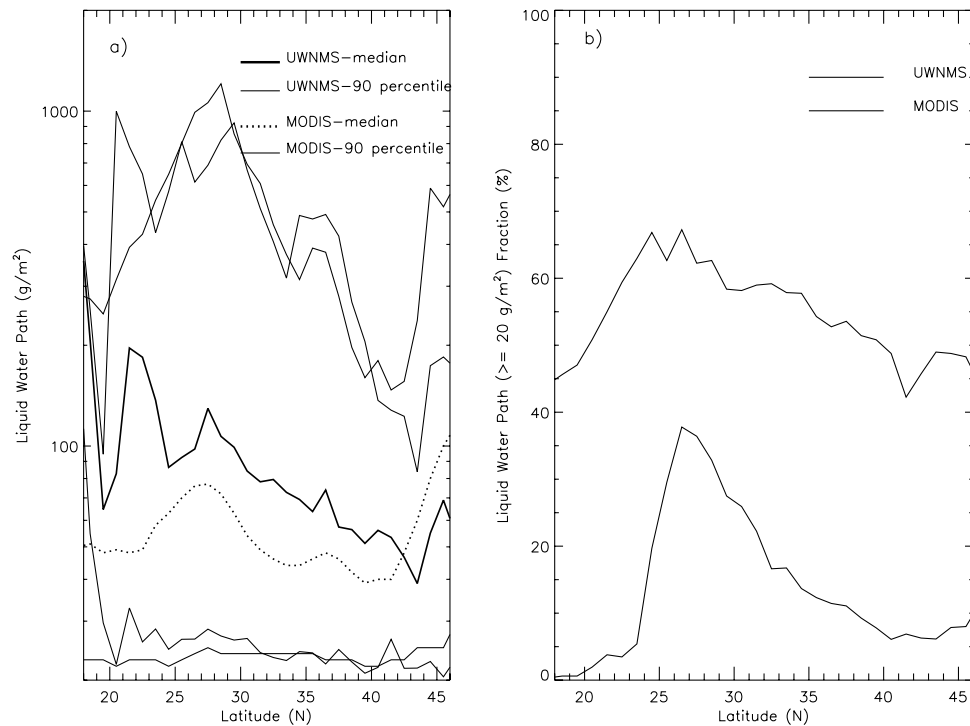


Figure 4. (a) Latitudinal variations of liquid water path (g/m^2) calculated from the UWNMS results (solid) and the MODIS data (dashed). The median and 90 percentiles are determined from liquid water path of more than $20 \text{ g}/\text{m}^2$ at each latitudinal bin. (b) Latitudinal variations of liquid water ($>20 \text{ g}/\text{m}^2$) fraction (%).

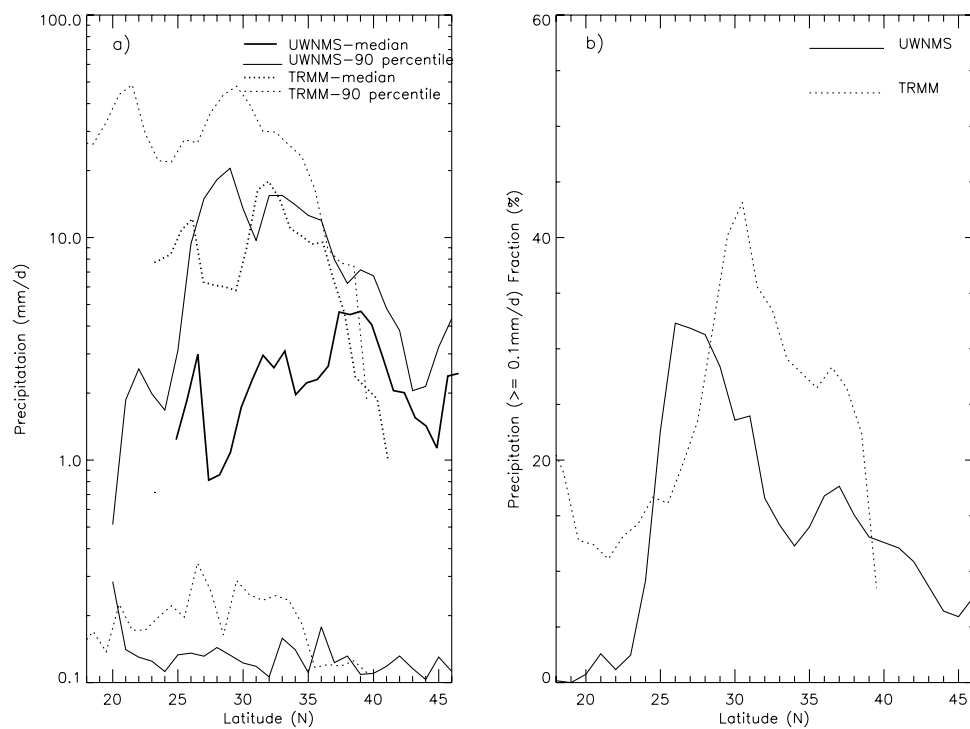


Figure 5. (a) Latitudinal variations of precipitation rate (mm/d) calculated from the UWNMS results (solid) and derived based on the TRMM data (dashed). The median and 90 percentiles are determined from precipitation rate of more than $0.1 \text{ mm}/\text{d}$. (b) Latitudinal variations of precipitation ($>0.1 \text{ mm}/\text{d}$) fraction (%).

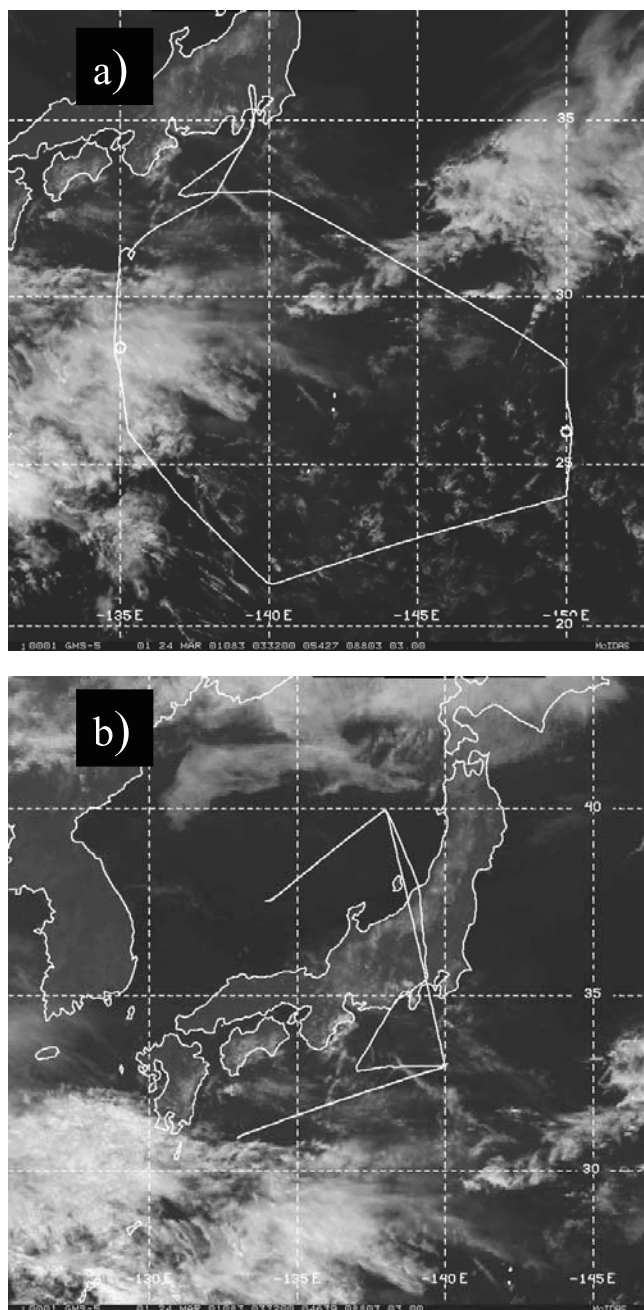


Figure 6. Satellite GMS-5 visible channel images at 0323 UT 24 March superimposed by (a) DC-8 flight 14 and (b) P-3B flight 16 flight tracks. The geolocations of the images are $(132^{\circ}\text{E}–152.5^{\circ}\text{E}, 20^{\circ}\text{N}–37.5^{\circ}\text{N})$ and $(125^{\circ}\text{E}–147.5^{\circ}\text{E}, 26^{\circ}\text{N}–44^{\circ}\text{N})$ for Figures 6a and 6b, respectively. The satellite images are provided by the University of Hawaii, the NASA Marshall Space Flight Center, and the NASA GTE Project Office.

acts as a medium for chemical reactions and also provides pathways for chemical substances to get incorporated into ice phase. Precipitation is a removal process for chemical substances with large solubility such as SO_2 , sulfate and H_2O_2 . To evaluate the UWNMS cloud prediction we compare the predicted vertically integrated liquid water path (LWP) with that derived from the data obtained from the

MODIS instrument on board the Terra platform. The MODIS LWP data sets ($15^{\circ}\text{N}–50^{\circ}\text{N}$ and $115^{\circ}\text{E}–150^{\circ}\text{E}$) used here are taken from the level 3 Atmospheric Daily Global Product ($1^{\circ} \times 1^{\circ}$ cells on an equal-angle grid). The 0000 UT UWNMS LWP predictions, which are closest to MODIS (Terra) overpass, are used in the comparison. Both data sets are sorted into 35 latitudinal bins between 15°N and 50°N with 1° spacing. LWP of 20 g/m^2 and greater is considered to effectively contribute to the sulfate in-cloud production. Grid volume with $\text{LWP} < 20 \text{ g/m}^2$ is not included in the analysis. The resulting number of sample points considered varies from 20 to 330. Figure 4a shows the comparison of the latitudinal variation of LWP between UWNMS and MODIS for the simulation period. Median, upper, and lower 90 percentiles of LWP ($\geq 20 \text{ g/m}^2$) are shown. Both UWNMS and MODIS LWP are highly variable with latitude. The peaks at $\sim 21^{\circ}\text{N}$ in the UWNMS LWP curves are not observed. This is, however, statistically insignificant because there are few predicted points in this latitude range. Except for the lower latitudes, UWNMS generally captures the latitudinal variation of LWP. The fraction of LWP exceeding 20 g/m^2 in the domain is plotted as a function of latitude in Figure 4b. This comparison clearly indicates that the UWNMS liquid water is

Predicted Sulfate Distribution at 06Z March 24, 2001

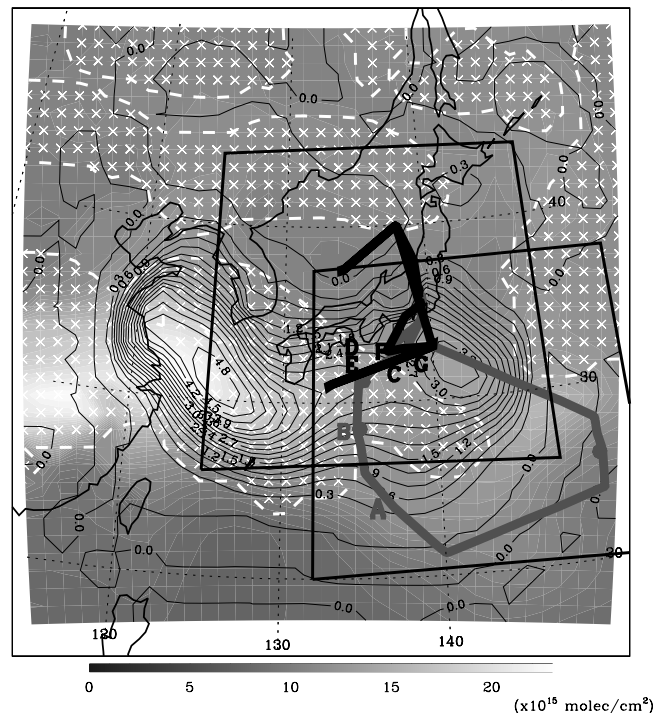


Figure 7. Vertically integrated sulfate S(VI)_a (colored contours), sulfate produced via in-cloud processing (solid black contours with a contour interval of $0.3 \times 10^{15} \text{ molec/cm}^2$), cloud water (liquid plus ice) path of 1 g/m^2 (dashed white line filled with white crosses for cloud water path $> 1 \text{ g/m}^2$) for 0600 UT 24 March 2001 and flight tracks (DC-8 flight 14, bold gray; P-3B flight 16, bold black). The A, B in gray and C–G in black denote the geolocations of the corresponding letters in Figures 8 and 9. See color version of this figure at back of this issue.

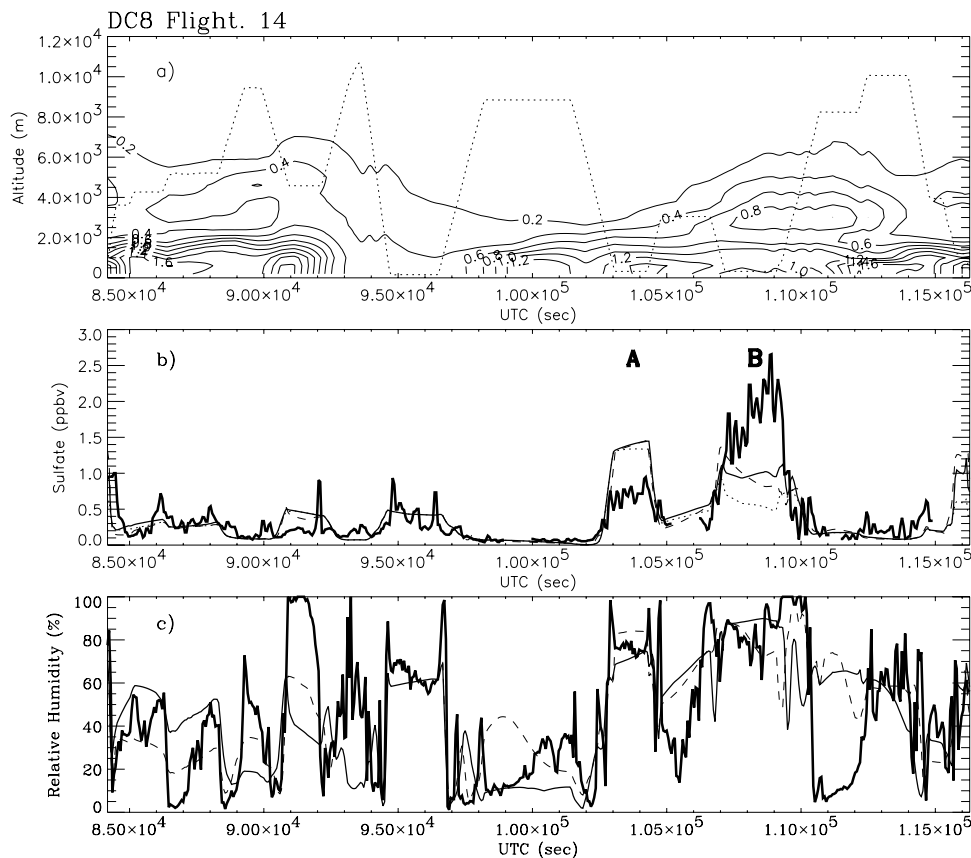


Figure 8. (a) Vertical cross section of sulfate $S(VI)_a$ (solid contours) along the DC-8 flight 14 flight track (the flight altitude is indicated by a dotted line). The contour interval is 0.2 ppbv. (b) Time series of sulfate mixing ratios along the flight track (simulated $S(VI)_a$, thin solid; simulated $S(VI)_{trc}$, dotted; measured, bold solid; simulated $S(VI)$ at higher resolution, dashed). (c) Time series of relative humidity along the flight track (simulated, thin solid; measured, bold solid; simulated at higher resolution, dashed). Note that there is no value for the simulation at high resolution between 9.30×10^4 and 9.75×10^4 s because the flight track is outside the model domain.

distributed in a more confined area ($25^\circ N$ – $32^\circ N$) than MODIS LWP, which shows a broader spread in latitude. The underestimate in the predicted liquid water frequency south of $24^\circ N$ may be due to a lack of explicit inflow of liquid water through the model boundaries. In the simulated atmosphere most clouds in the north of $40^\circ N$ are in the ice phase. Despite these discrepancies, both UWNMS and MODIS LWP clearly show the signatured storms passing at about $28^\circ N$ during the simulation period.

[30] UWNMS daily precipitation was calculated using 12-hour accumulated precipitation. Latitudinally binned UWNMS daily precipitation is compared with precipitation estimates based on the Tropical Rainfall Measuring Mission (TRMM) data (available up to 40°) [Huffman *et al.*, 1995] in Figure 5. The precipitation estimates from the TRMM data show distinctive peaks at two latitudinal ranges, $18^\circ N$ – $22^\circ N$ and $27^\circ N$ – $32^\circ N$. The high precipitation rate (Figure 5a) and small precipitation fraction (Figure 5b) suggest episodic intensive rain events at $18^\circ N$ – $22^\circ N$, whereas the high precipitation rate and high precipitation fraction suggest frequent intensive rain events at $27^\circ N$ – $32^\circ N$. The simulation results show similar intensive rain events at $27^\circ N$ – $32^\circ N$. Additionally, the simulation results show episodic rain events (high intensity in limited areas)

at $32^\circ N$ – $37^\circ N$. The simulated precipitation is by a factor of 5 lower than derived. This is due to the limitations of the microphysical representation in the model and the coarse horizontal resolution.

4.2. In-Cloud Production of Sulfate

4.2.1. A Case Study for DC8 Flight 14 and P3B Flight 16

[31] On 24 March 2001, two aircraft flights were conducted in the southeast of Japan and across the Honshu island, Japan, by DC-8 flight 14 and P-3B flight 16, respectively. Figures 6a and 6b show the satellite GMS-5 visible channel images taken at 0323 UT 24 March, which is close to the halfway of these flights in time, superimposed by these two flight tracks (DC-8 flight 14 and P-3B flight 16 flight tracks in Figures 6a and 6b, respectively). These two satellite images depict deep convective activity extending from farther west of $120^\circ E$ to $140^\circ E$, sparse convective clouds between $140^\circ E$ and $145^\circ E$, and a moderately convective cloud band farther east of $145^\circ E$ in the south of the Japan islands. The convective clouds were observed to have formed over the eastern China on the previous day and developed eastward to $140^\circ E$ by the time of the flights. This is one of a few intensive thunderstorms observed in the

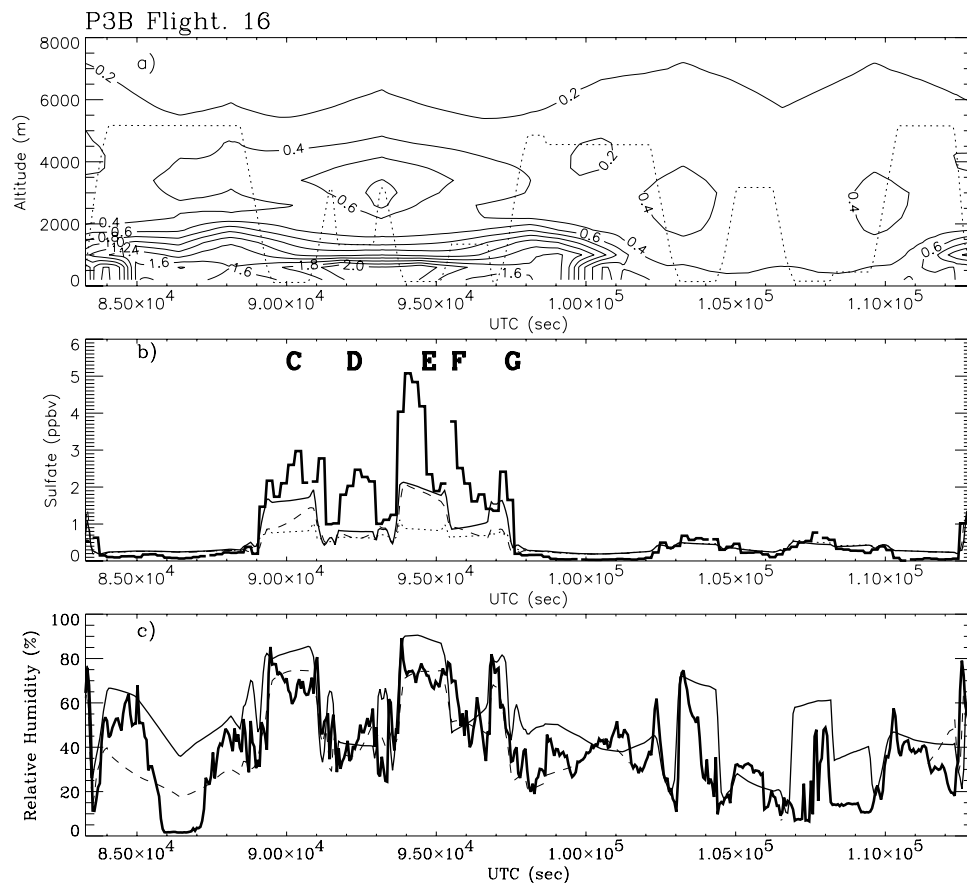


Figure 9. Same as Figure 8 except for P-3B flight 16. Note that there is no value for the simulation higher resolution between 1.02×10^5 and 1.15×10^5 s because the flight track is outside the model domain.

vicinity of the in situ measurements during TRACE-P. The flight tracks superimposed on the satellite images show both flights partly intercepted the cloudy regions to the south of Japan islands and successfully sampled cloud-influenced air. Figure 7 shows the predicted distributions of column sulfate (colored contours) and cloud water (liquid plus ice) path in excess of 1 g/m^2 (an area confined with a white bold dashed line and filled with white crosses) for 0600 UT 24 March. The two boxes indicated by a black solid line in Figure 7 show the positions of the satellite images in Figure 6 (the lower right box for Figure 6a and the upper left box for Figure 6b). The sulfate released into air after being produced via in-cloud processing is derived by subtracting $S(\text{VI})_{\text{irc}}$ from $S(\text{VI})_a$. The distribution of vertically integrated amounts of this sulfate is shown with contours in Figure 7. The simulated cloud fields are found over the eastern part of China to 135°E within the latitudinal ranges between 25°N and 35°N and in the east of 140°E between 30°N and 40°N , which are in good agreement with those in the satellite images (taken about 2.5 hours earlier) except for the slight displacement of the northeastern portion of the clouds toward the north in the prediction. The model results show the significant amount of sulfate off the coast of China extending across the east China Sea. The significantly high amounts of sulfate (1–4.2 ppbv) that has been released into air after being produced via in-cloud processing are seen where the deep convective activity is

observed (centered at 30°N , 125°E). The second peak of this sulfate is seen in the east of the main peak at around 33°N and 142°E . Figure 8a is a contour plot of the vertical cross section of the simulated sulfate ($S(\text{VI})_a$) along the flight track of DC-8 flight 14. The altitude of the aircraft is indicated by a dotted line. The visible aerosol scattering ratio measured using UV DIAL (Differential Absorption Lidar) system on DC-8 reveals the vertical profile of aerosols for this flight (not shown) [Browell *et al.*, 2003]. It shows high aerosol levels throughout the boundary layer, a relatively high aerosol level at the altitude of 6 km at between 8.8×10^4 and 9.0×10^4 s (UTC), and an elevated level of an aerosol layer at about 7 km at between 1.10×10^5 and 1.14×10^5 s (UTC). The good agreement between the simulated sulfate vertical profile and the vertical profile of the visible aerosol scattering ratio suggests that the model qualitatively captures the sulfate vertical distribution for this flight. Figures 8b and 8c show the sulfate ($S(\text{VI})_a$) mixing ratio and relative humidity of simulated (thin solid line) and measured (bold solid line) at the same vertical slice as in Figure 8a. Figures 9a–9c show corresponding data along the P-3B flight 16 flight track. Considerably elevated sulfate mixing ratios (1–5 ppbv) were observed in the both flights as denoted A–G in Figures 8b and 9b. The geolocations of these peaks are shown in Figure 7. All of the peaks are observed in the boundary layer except for the peak D and F, which are observed at the altitude of 1.5 km. The high

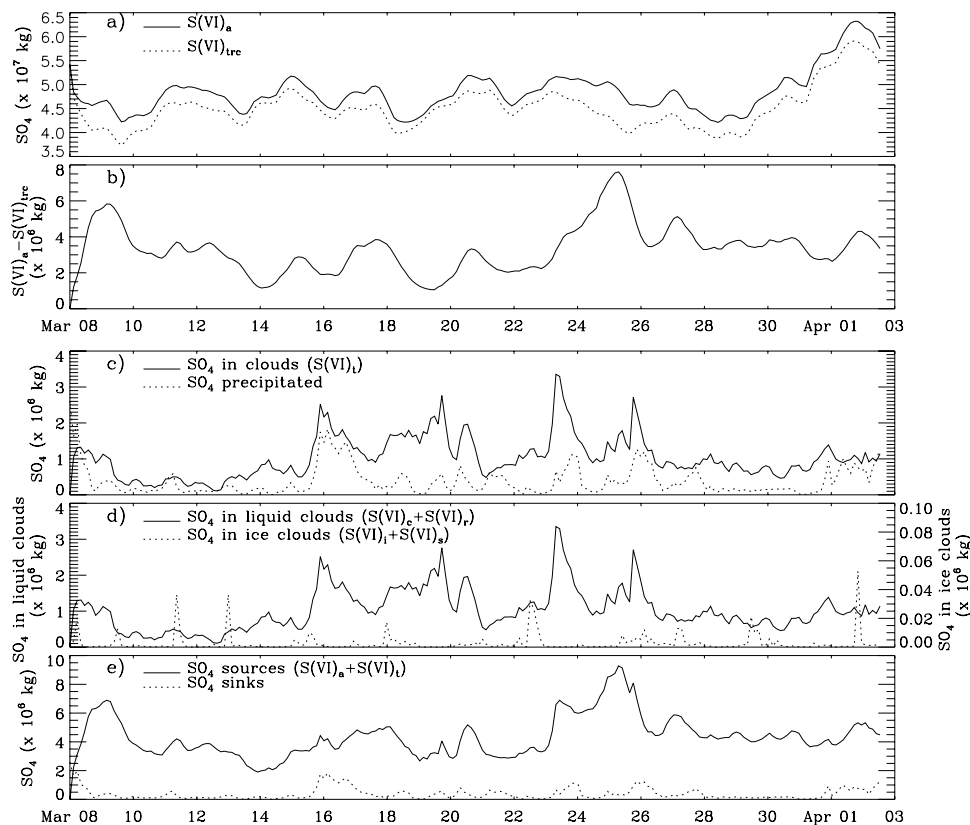


Figure 10. (a) Time series of the volume-integrated sulfate ($S(VI)_a$) mass in the regional domain (solid) and the volume-integrated idealized sulfate tracer ($S(VI)_{trc}$) mass (dashed). (b) Difference between two curves in Figure 10a. (c) Instantaneous sulfate mass contained in clouds $S(VI)_t$ (solid) and sulfate mass lost through rainout (dashed). (d) Instantaneous sulfate mass contained in liquid cloud ($S(VI)_c + S(VI)_l$) and in ice clouds ($S(VI)_i + S(VI)_s$). (e) Sum of the volume-integrated masses of $S(VI)_a$ and $S(VI)_t$ (solid) and the sulfate mass lost through rainout (dashed). Note that the y axis for $S(VI)$ in liquid clouds is on the left side of the plot and that for $S(VI)$ is on the right side.

relative humidity (90–100%) measured (Figure 8c) at B and satellite image (Figure 6a) indicate the air sampled within the cloud. The mixing ratios at C, E, and G are probably near the cloud edge or outside the cloud since the relative humidity is moderately high (~80%) but not as high as that found within clouds. The comparisons of the sulfate mixing ratios between the simulation and the measurements show an excellent agreement in the background sulfate mixing ratios. The simulated sulfate mixing ratios at B–G are much smaller than those of the measured, while that at A is twice higher than that measured. The SO_2 mixing ratio at E is considerably underestimated in the simulation, and consequently the sulfate mixing ratio is underestimated. The model misses capturing the peaks at D and F, which are observed at the altitude of 1.5 km. In addition to the $S(VI)_a$ mixing ratios, $S(VI)_{trc}$ mixing ratios, which are not subject to in-cloud processing, are plotted in Figures 8b and 9b. Comparing the $S(VI)_a$ mixing ratios with the $S(VI)_{trc}$ mixing ratios, there is a significant enhancement of $S(VI)_a$ at B, C, E, and G. Considering the relative humidity of 90–100% at B, the enhancement of sulfate is due to in-cloud processing. The sulfate at C, E, and G is also produced in clouds that have evaporated by the time of the measurements. There is little enhancement in sulfate mixing ratios from $S(VI)_{trc}$ at A, and therefore the sulfate is suggested to

be produced by other than in-cloud processing. In order to see the effects of horizontal resolution on the sulfate production, a simulation at higher horizontal resolution (30 km \times 30 km) and the same vertical resolution (0.4 km) was conducted for this case study. The initial and lateral boundary conditions were taken from the simulated results at the coarse horizontal resolution. $S(VI)_a$ mixing ratios and relative humidity are shown in a dashed line in Figures 8b, 8c, 9b, and 9c. A significant improvement in relative humidity is seen. $S(VI)_a$ mixing ratios, however, show little change. At the peaks C and G in Figure 9b, the $S(VI)_a$ high-resolution mixing ratio predictions show worse agreement than the lower-resolution results.

4.2.2. Net Sulfate Production

[32] The sulfate produced via in-cloud processing in the east Asian region for 7 March to 3 April 2001 is now estimated by integrating the total sulfate within the regional domain. The sulfate produced via in-cloud processing may be released into air, remain in clouds, or be lost through precipitation. Figure 10a shows time series of the volume-integrated $S(VI)_a$ and $S(VI)_{trc}$ mass. The difference (Figure 10b) between these two curves reflects the volume-integrated sulfate mass that is released into air after being produced in clouds. Figure 10c shows the sulfate mass remaining in clouds (the volume-integrated $S(VI)_t$ mass

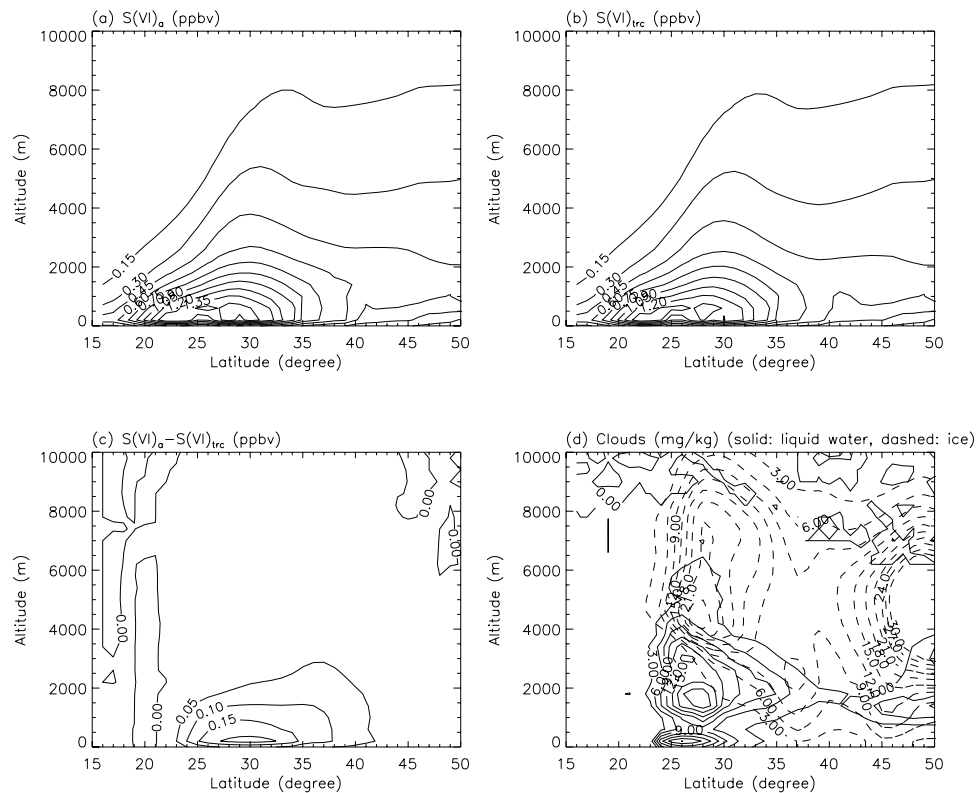


Figure 11. (a) Zonal averaged mixing ratios of $S(VI)_a$. (b) Zonal average mixing ratios of the idealized sulfate tracer $S(VI)_{re}$. (c) Differences between Figures 11a and 11b. (d) Zonal averaged cloud mixing ratios (liquid water, solid; ice, dashed).

indicated by a solid line) and the sulfate mass lost through precipitation (dotted line). The sulfate mass released into air after being produced in clouds varies in the ranges between 1.5×10^6 kg and 7.5×10^6 kg (Figure 10b), remaining in clouds is 0.2×10^6 to 3.5×10^6 kg (solid line in Figure 10c), and being precipitated is 0.01×10^6 to 1.8×10^6 kg (dotted line in Figure 10c). The fate of sulfate in clouds is determined by the microphysical properties of the cloud and the local meteorological conditions. If the cloud is nonprecipitating, then the sulfate in the cloud remains in the atmosphere or is removed through dry deposition, which is not an effective pathway of sulfate removal [Davis *et al.*, 2003]. If the cloud produces rain, the sulfate may be lost through rainout (acid rain). As mentioned in section 4.2.1, the intensive deep convective activity was observed on 24 March. During this episode, the model predicts that a large amount of sulfate was produced in clouds and released into air as the cloud evaporated. The time series in Figure 10b clearly indicates this event as a peak between 24 and 26 March. Sulfate remaining inside the clouds rapidly increases at the beginning of the convective period (23 March), and decreases as the clouds evaporate (late 23 March) (solid line in Figure 10c). The curve of sulfate precipitated (dotted line in Figure 10c) indicates the storm on 24 March did not produce particularly severe acid rain since the large portion of sulfate produced in clouds may have been released into air. In contrast to the storm on 24 March, the model predicts that the clouds formed between 15 and 16 March do not release a large amount of sulfate into air. Instead, a large portion of sulfate is precipitated. Figure 10d shows the volume-

integrated $S(VI)$ mass found in liquid clouds (i.e., cloud drops and raindrops) and in ice clouds (i.e., ice crystals and snow). The contribution of $S(VI)$ in liquid clouds is 2 orders of magnitude larger than that in ice clouds. Figure 10e shows the sum of the sulfate mass suspended in air ($S(VI)_a$) and that in clouds ($S(VI)_i$) as a local sulfate source (solid line), and also the sulfate mass lost through precipitation as a local sulfate sink (dotted line). Throughout the simulation the total sulfate source exceeds the sink by far. This is compared with the global sulfate sources and sinks. Davis *et al.* [2003] show the global sources and sinks of sulfate obtained from seven global sulfur model runs. The median value of the sulfate source due to in-cloud processing obtained from these global models is 40.0 Tg S/yr whereas the median value of the sulfate sink due to wet deposition is 44.5 Tg S/yr. According to these results, the global sulfate loss due to wet deposition exceeds the global source due to in-cloud processing by 4.5 Tg S/yr. Figure 10e shows that in the east Asian region the sulfate source due to in-cloud processing is much larger than the sink due to wet deposition, and therefore contribution to a net sulfate input to the atmosphere. The comparisons of the simulated cloud and precipitation fields with the satellite retrieved values have shown the considerable underestimates of cloud and precipitation fractions in the simulation. The underestimate of cloud fraction introduces a negative bias to sulfate mass produced in clouds (the source) while the underestimate of precipitation fraction introduces a negative bias to sulfate mass precipitated (the sink). Assessing the impact of these biases on the sulfate budget is beyond the scope of this study.

[33] Figures 11a and 11b are the zonal average of $S(VI)_a$ and $S(VI)_{trc}$ mixing ratios, respectively, between 15°N and 50°N for 7 March to 3 April 2001. Both show high mixing ratios (1.65 ppbv for $S(VI)_a$ and 1.35 ppbv for $S(VI)_{trc}$) at 24°N – 29°N . The difference between these two distributions, which accounts for the sulfate mixing ratio released into air after produced in clouds, is shown in Figure 11c. This shows that sulfate is released from clouds into the atmosphere below 1 km. The maximum difference (0.15 ppbv) between $S(VI)_a$ and $S(VI)_{trc}$ is seen at around 30°N , while the maximum cloud liquid water mixing ratio is found at 26°N (Figure 11d). The possible cause of this difference is that chemical species are removed through precipitation. This is consistent with the maximum precipitation rate in the simulated fields at 25°N – 27°N (see Figure 5b). The removal through precipitation is most effective for H_2O_2 since H_2O_2 is highly water soluble. As a result, amounts of H_2O_2 available for the oxidation is small relative to liquid water amounts at about 30°N and thus limits the conversion of SO_2 to sulfate.

5. Summary and Conclusions

[34] The objective of this study was to estimate the contribution of the sulfate in-cloud production to the total sulfate in east Asia during the TRACE-P period. A regional simulation of the sulfate transport for the TRACE-P period was conducted using UWNMS with an aqueous sulfur chemistry model. First, the model performance in predicting distributions of SO_2 , sulfate, H_2O_2 , liquid cloud water and precipitation was assessed by comparing with in situ measurements and satellite observations. The comparisons revealed the overestimate of the sulfate mixing ratios by 20% between 1 and 6 km and the underestimates by 30% near the surface and by 50% above 6 km. The predictions overestimated SO_2 and H_2O_2 mixing ratios by a factor of 1.2–3 at almost all altitude and latitude bins. Despite these discrepancies, the relative patterns of their vertical and latitudinal variations were in good agreement with in situ measurements. The comparisons of liquid water path between the simulation and the satellite observation show that the simulated cloud frequencies were low. The precipitation rates are by a factor of 5 smaller than those derived based on the TRMM data. This possibly altered the sulfate budget in the lower troposphere.

[35] A case study was conducted for 24 March 2001, when air influenced by a deep convective storm was advected from the east coast of China to the south of Japan islands. The regional simulation identified the enhancement of sulfate due to in-cloud processing by comparing the standard sulfate mixing ratios with the idealized sulfate tracer mixing ratios. However, it underestimated the mixing ratios of sulfate that was released in air by a factor of 2. The effects of horizontal resolution were examined by using higher resolution $30\text{ km} \times 30\text{ km}$ for this case study. The improvement in relative humidity fields was seen in the higher resolution run, but there was no improvement in the sulfate fields. Volume integrated sulfate mass in the regional domain was calculated during the TRACE-P period. The total sulfate mass varied between $4.25 \times 10^7\text{ kg}$ and $6.4 \times 10^7\text{ kg}$ due to transport, in-cloud production and removal through precipitation. Instantaneous sulfate mass of

0.2×10^6 to $3.5 \times 10^6\text{ kg}$ was predicted in clouds. The sulfate mass in ice clouds was 2 orders of magnitude smaller than that in liquid clouds. The ice clouds were found to be an ineffective reservoir of sulfate. The fate of this in-cloud sulfate is determined by the microphysical properties of the cloud and the local meteorological conditions. This study showed that the sulfate input to the atmosphere exceeds the sulfate removed from the atmosphere through precipitation in the east Asian region during the TRACE-P. Consequently, east Asia in spring can be an important source region of sulfate and thus can offset the sulfate loss in other regions of the globe. This should not be extrapolated to other seasons since the east Asian region in spring has more favorable conditions for sulfate in-cloud production than other regions of the globe. The quantification of the sulfate input in east Asia requires accurate predictions of meteorological variables. Therefore errors in the predicted clouds and precipitation can result in a significant impact on the sulfate budget. SO_2 dry deposition, sulfate and DMS emissions, the oxidation of $S(VI)$ by ozone, which is imported from the RAQMS global model, will be included in subsequent sulfate model development.

[36] **Acknowledgments.** Support for this work was provided by the NASA Atmospheric Chemistry Modeling and Analysis Program (ACMAP) and the NASA Langley Research Center (LaRC) Creativity and Innovation Program. Brian Heikes, Daniel O'Sullivan, and Julie Snow are thanked for sharing their hydrogen peroxide. One of the authors (C. Kittaka) thanks T. D. Fairlie for his comments and suggestions in preparing this manuscript.

References

- Barth, M. C., A. L. Stuart, and W. C. Skamarock (2001), Numerical simulations of the July 10, 1996, Stratospheric-Tropospheric Experiment: Radiation, Aerosols, and Ozone (STERAO)-Deep Convection experiment storm: Redistribution of soluble tracers, *J. Geophys. Res.*, *106*, 12,381–12,400.
- Binkowski, F. S., and S. J. Roselle (2003), Models-3 Community Multi-scale Air Quality (CMAQ) model aerosol component: 1. Model description, *J. Geophys. Res.*, *108*(D6), 4183, doi:10.1029/2001JD001409.
- Borys, R. D., E. E. Hindman, and P. J. Demott (1988), The chemical fractionation of atmospheric aerosol as a result of snow crystal formation and growth, *J. Atmos. Chem.*, *7*, 213–239.
- Browell, E. V., et al. (2003), Large-scale ozone and aerosol distributions, air mass characteristics, and ozone fluxes over the western Pacific Ocean in late winter/early spring, *J. Geophys. Res.*, *108*(D20), 8805, doi:10.1029/2002JD003290.
- Calvert, J. G., et al. (1985), Chemical mechanisms of acid generation in the troposphere, *Nature*, *317*, 27–35.
- Carmichael, G., et al. (2003), Regional-scale chemical transport modeling in support of intensive field experiments: Overview and analysis of the TRACE-P observations, *J. Geophys. Res.*, *108*(D21), 8823, doi:10.1029/2002JD003117.
- Chin, M., R. B. Rood, S.-J. Lin, J.-F. Müller, and A. M. Thompson (2000a), Atmospheric sulfur cycle simulated in the global model GOCART: Model description and global properties, *J. Geophys. Res.*, *105*, 24,671–24,687.
- Chin, M., et al. (2000b), Atmospheric sulfur cycle simulated in the global model GOCART: Comparison with field observations and regional budgets, *J. Geophys. Res.*, *105*, 24,689–24,712.
- Chin, M., et al. (2002), Tropospheric aerosol optical thickness from the GOCART model and comparisons with satellite and sun photometer measurements, *J. Atmos. Sci.*, *59*, 461–483.
- Chin, M., et al. (2003), A global aerosol model forecast for the ACE-Asia field experiment, *J. Geophys. Res.*, *108*(D23), 8654, doi:10.1029/2003JD003642.
- Crawford, J., et al. (2003), Clouds and trace gas distributions during TRACE-P, *J. Geophys. Res.*, *108*(D21), 8818, doi:10.1029/2002JD003177.
- Davis, D. D., G. Chen, and M. Chin (2003), Atmospheric sulfur, in *Handbook of Weather, Climate, and Water: Atmospheric Chemistry, Hydrology, and Societal Impacts*, edited by T. D. Potter and B. R. Colman, pp. 125–156, John Wiley, Hoboken, N. J.

- Dibb, J. E., R. W. Talbot, E. Scheuer, G. Seid, M. A. Avery, and H. B. Singh (2003), Aerosol chemical composition in Asian Continental outflow during TRACE-P: Comparison to PEM-West B, *J. Geophys. Res.*, *108*(D21), 8815, doi:10.1029/2002JD003111.
- Dickerson, R. R. (1987), Thunderstorms: An important mechanism in the transport of air pollutants, *Science*, *235*, 460–465.
- Diehl, K., S. K. Mitra, and H. R. Pruppacher (1998), A laboratory study on the uptake of HCl, HNO₃, and SO₂ gas by ice crystals and the effect of these gases on the evaporation rate of the crystals, *Atmos. Environ.*, *47*–*48*, 235–244.
- Eisele, F. L., et al. (2003), Summary of measurement intercomparisons during TRACE-P, *J. Geophys. Res.*, *108*(D20), 8791, doi:10.1029/2002JD003167.
- Emanuel, K. A. (1991), A scheme for representing cumulus convection in large-scale models, *J. Atmos. Sci.*, *48*, 2313–2335.
- Flatau, P., G. J. Tripoli, J. Verlinde, and W. Cotton (1989), The CSU RAMS cloud microphysics module: General theory and code documentation, *Tech. Rep. 451*, Dep. of Atmos. Sci., Colo. State Univ., Fort Collins.
- Hitchman, M. H., M. L. Buker, G. J. Tripoli, R. B. Pierce, J. A. Al-Saadi, E. V. Browell, and M. A. Avery (2004), A modeling study of an east Asian convective complex during March 2001, *J. Geophys. Res.*, *109*, doi:10.1029/2003JD004312, in press.
- Hoppel, W. A., and G. M. Frick (1990), Submicron aerosol size distributions measured over the tropical and South Pacific, *Atmos. Environ., Part A*, *24*, 569–645.
- Huffman, G. J., R. F. Adler, B. Rudolf, U. Schneider, and P. R. Keehn (1995), Global precipitation estimates based on a technique for combining satellite-based estimates, rain gauge analysis, and NWP model precipitation information, *J. Clim.*, *8*, 1284–1295.
- Intergovernmental Panel on Climate Change (IPCC) (2001), *Climate Change 2001: The Scientific Basis*, edited by J. T. Houghton et al., Cambridge Univ. Press, New York.
- Jacob, D. J., et al. (2003), The Transport and Chemical Evolution over the Pacific (TRACE-P) mission: Design, execution and overview of results, *J. Geophys. Res.*, *108*(D20), 9000, doi:10.1029/2002JD003276.
- Jacobson, M. Z. (1997), Development and application of a new air pollution modeling system-II. Aerosol module structure and design, *Atmos. Environ.*, *31*, 131–144.
- Jaeglé, L., et al. (2003), Sources and budgets for CO and O₃ in the northeastern Pacific during the spring of 2001: Results from the PHOBEA-II Experiments, *J. Geophys. Res.*, *108*(D20), 8802, doi:10.1029/2002JD003121.
- Kiley, C. M., et al. (2003), An intercomparison and evaluation of aircraft-derived and simulated CO from seven chemical transport models during the TRACE-P experiment, *J. Geophys. Res.*, *108*(D21), 8819, doi:10.1029/2002JD003089.
- Kittaka, C. (2001), A modeling study of transport and transformation of sulfur species in a deep convective cloud, Ph.D. thesis, Univ. of Wis.-Madison, Madison.
- Kreidenweis, S. M., Y. Zhang, and G. R. Taylor (1997), The effects of clouds on aerosol and chemical species production and distribution: 2. Chemistry model description and sensitivity analysis, *J. Geophys. Res.*, *102*, 23,867–23,882.
- Mitchell, D. L., and D. Lamb (1989), Influence of riming on the chemical composition of snow in winter orographic snow, *J. Geophys. Res.*, *94*, 14,831–14,840.
- Müller, J.-F., and G. Brasseur (1995), IMAGES: A three-dimensional chemical transport model of the global troposphere, *J. Geophys. Res.*, *100*, 16,445–16,490.
- Pickering, K. E., et al. (1996), Convective transport of biomass burning emissions over Brazil during TRACE-A, *J. Geophys. Res.*, *101*, 23,993–24,012.
- Pierce, R. B., et al. (2003), Regional Air Quality Modeling System (RAQMS) predictions of the tropospheric ozone budget over East Asia, *J. Geophys. Res.*, *108*(D21), 8825, doi:10.1029/2002JD003176.
- Price, H. U., D. A. Jaffe, P. V. Doskey, I. McKendry, and T. L. Anderson (2003), Vertical profiles of O₃, aerosols, CO and NMHCs in the northeast Pacific during the TRACE-P and ACE-ASIA experiments, *J. Geophys. Res.*, *108*(D20), 8799, doi:10.1029/2002JD002930.
- Rasch, P. J., N. M. Mahowald, and B. E. Maton (1997), Representations of transport, convection, and the hydrologic cycle in chemical transport models: Implications for the modeling of short lived and soluble species, *J. Geophys. Res.*, *102*, 28,127–28,138.
- Schwartz, S. E. (1988), Mass-transport limitation to the rate of in-cloud oxidation of SO₂: Re-examination in the light of new data, *Atmos. Environ.*, *22*, 2491–2499.
- Seinfeld, J. H., and S. N. Pandis (1998), *Atmospheric Chemistry and Physics*, 1326 pp., Wiley-Interscience, Hoboken, N. J.
- Streets, D. G., et al. (2003), An inventory of gaseous and primary aerosol emissions in Asia in the year 2000, *J. Geophys. Res.*, *108*(D21), 8809, doi:10.1029/2002JD003093.
- Stuart, A. L., and M. Z. Jacobson (2003), A timescale investigation of volatile chemical retention during hydrometeor freezing: Nonrime freezing and dry growth riming without spreading, *J. Geophys. Res.*, *108*(D6), 4178, doi:10.1029/2001JD001408.
- Tripoli, G. J. (1992), A nonhydrostatic numerical model designed to simulate scale interaction, *Mon. Weather Rev.*, *120*, 1342–1359.
- Tripoli, G. J., and W. R. Cotton (1981), The use of ice-liquid water potential temperature as a thermodynamic variable in deep atmospheric models, *Mon. Weather Rev.*, *109*, 1094–1102.
- Tu, F. H., et al. (2003), Dynamics and transport of sulfur dioxide over the Yellow Sea during TRACE-P, *J. Geophys. Res.*, *108*(D20), 8790, doi:10.1029/2002JD003227.
- Weber, R. J., et al. (2003), New particle formation in anthropogenic plumes advecting from Asia observed during TRACE-P, *J. Geophys. Res.*, *108*(D21), 8814, doi:10.1029/2002JD003112.

B. E. Anderson and J. H. Crawford, NASA Langley Research Center, Mail Stop 483, Hampton, VA 23681-2199, USA. (bruce.e.anderson@nasa.gov; james.h.crawford@nasa.gov)

A. R. Bandy, Chemistry Department, Drexel University, 32nd and Chestnut Streets, Philadelphia, PA 19104, USA. (bandyar@drexel.edu)

M. Chin, NASA Goddard Space Flight Center, Code 916, Greenbelt, MD 20771, USA. (mian.chin@nasa.gov)

M. H. Hitchman, D. R. Johnson, and G. J. Tripoli, Department of Atmospheric and Oceanic Sciences, University of Wisconsin-Madison, 1225 W. Dayton Street, Madison, WI 53706, USA. (matt@aos.wisc.edu; donj@ssec.wisc.edu; tripoli@aos.wisc.edu)

C. Kittaka, Science Applications International Corporation, NASA Langley Research Center, Mail Stop 401B, Hampton, VA 23681-2199, USA. (fn.c.kittaka@larc.nasa.gov)

R. B. Pierce, NASA Langley Research Center, Mail Stop 401B, Hampton, VA 23681-2199, USA. (robert.b.pierce@nasa.gov)

R. W. Talbot, EOS, Morse Hall, University of New Hampshire, Durham, NH 03824, USA. (robert.talbot@unh.edu)

R. J. Weber, School of the Earth and Atmospheric Sciences, Georgia Institute of Technology, Atlanta, GA 30332, USA. (rweber@eas.gatech.edu)

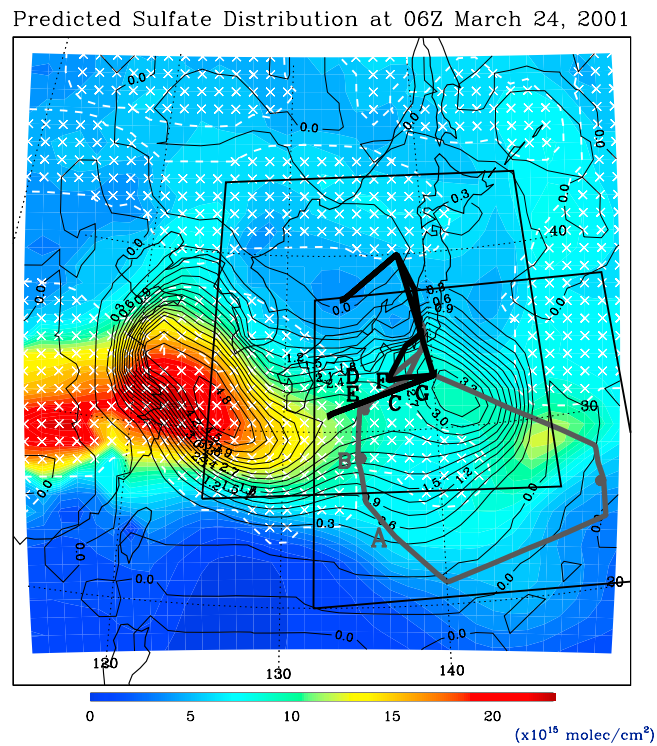


Figure 7. Vertically integrated sulfate $S(\text{VI})_a$ (colored contours), sulfate produced via in-cloud processing (solid black contours with a contour interval of 0.3×10^{15} molec/cm²), cloud water (liquid plus ice) path of 1 g/m^2 (dashed white line filled with white crosses for cloud water path $>1 \text{ g/m}^2$) for 0600 UT 24 March 2001 and flight tracks (DC-8 flight 14, bold gray; P-3B flight 16, bold black). The A, B in gray and C–G in black denote the geolocations of the corresponding letters in Figures 8 and 9.